Hindawi
Geofluids
Volume 2020, Article ID 5295490, 13 pages
https://doi.org/10.1155/2020/5295490

Research Article

Quantitative Characterization of Pore Connectivity and Movable Fluid Distribution of Tight Sandstones: A Case Study of the Upper Triassic Chang 7 Member, Yanchang Formation in Ordos Basin, China

Boli Wang[1,2] **Xisen Zhao**[3] **Wen Zhou**[1,2] **Bin Chang**[3] **and Hao Xu**[1,2]

[1]*State Key Laboratory of Oil and Gas Reservoir Geology and Exploitation (Chengdu University of Technology), Chengdu, Sichuan 610059, China*
[2]*College of Energy, Chengdu University of Technology, Chengdu, Sichuan 610059, China*
[3]*Research Institute, Shaanxi Yanchang Petroleum (Group) Co., Ltd., Xi'an, Shaanxi 710075, China*

Correspondence should be addressed to Wen Zhou; zhouw62@cdut.edu.cn and Hao Xu; haoxu777@qq.com

Received 3 September 2019; Accepted 7 January 2020; Published 23 January 2020

Academic Editor: Ling-Li Zhou

The pore connectivity and distribution of moveable fluids, which determines fluid movability and recoverable reserves, are critical for enhancing oil/gas recovery in tight sandstone reservoirs. In this paper, multiple techniques including high-pressure mercury intrusion porosimetry (MIP), nuclear magnetic resonance (NMR), scanning electron microscopy (SEM), and microcomputer tomography scanning (micro-CT) were used for the quantitative characterization of pore structure, pore connectivity, and movable fluid distribution. Firstly, sample porosity and permeability were obtained. Pore morphology and the 3D distribution of the pore structures were analyzed using SEM and micro-CT, respectively. The pore-size distribution (PSD) from NMR was generally broader than that from MIP because this technique simply characterized the connected pore volume, whereas NMR showed the total pore volume. Therefore, an attempt was made to calculate pore connectivity percentages of pores with different radii (<50 nm, 50 nm–0.1 μm, and 0.1 μm–1 μm) using the difference between the PSD obtained from MIP and NMR. It was found that small pores ($r < 0.05\,\mu$m) contributed 5.02%–18.00% to connectivity, which is less than large pores ($r > 0.05\,\mu$m) with contribution of 36.60%–92.00%, although small pores had greater pore volumes. In addition, a new parameter, effective movable fluid saturation, was proposed based on the initial movable fluid saturation from NMR and the pore connectivity percentage from MIP and NMR. The results demonstrated that the initial movable fluid saturation decreased by 14.16% on average when disconnected pores were excluded. It was concluded that the effective movable fluid saturation has a higher accuracy in evaluating the recovery of tight sandstone reservoirs.

1. Introduction

In recent years, unconventional fossil resources such as shale gas, coal-bedded methane, tight gas, and tight oil have derived remarkable success in North America and China [1–3]. The success of unconventional oil and gas exploration and development has resulted in fast growth in oil and gas production, which is based on the development of new techniques such as horizontal well drilling and hydraulic fracturing.

Unconventional oil and gas reservoirs, including shale gas, tight gas, and tight oil reservoirs, are characterized by low permeability and low porosity [3, 4]. The complex system of pores in tight sandstone makes it difficult to characterize pore structure and connectivity. Many researchers have tried to enhance oil recovery from these tight-rock reservoirs [5, 6]. These investigations have included quantitative characterization of pore structure using various techniques [7–9], connectivity analysis of tiny pores [10–14], and predictions of migration of movable fluids and oil/gas

production [15, 16]. Tight sandstone reservoirs have extremely complex pore systems and low recovery. To obtain a better understanding of the characteristics of these reservoirs, multiple techniques have been used to characterize the pore systems, including high-resolution scanning electron microscopy (SEM), low-temperature liquid nitrogen adsorption, high-pressure mercury intrusion porosimetry (MIP), computer tomography scanning (CT scanning), and nuclear magnetic resonance (NMR). These techniques have been combined to characterize pore structures of tight sandstone [7, 17, 18]. Among these techniques, MIP can reveal the petrophysical properties and pore-size distribution (PSD), CT scanning can illustrate the 3D distribution of pores, and NMR can describe the PSD and moveable fluids [13, 19]. Each technique has its own principles and limitations; therefore, researchers have generally combined these different techniques to accurately characterize PSD [7, 20–22].

Movable fluid saturation and connectivity of the pore system in a tight sandstone reservoir is critical for enhancing oil recovery. The connectivity of nanoscale and micron-scale pore systems has been discussed extensively [23–25]. Previous investigators analyzed connectivity using spontaneous imbibition (SI) and saturation tracer diffusion behaviors [5, 10, 11, 26]. However, the mercury intrusion method and spontaneous imbibition can only characterize interconnectivity, because external fluids cannot invade isolated pores. On the other hand, NMR is a radiation method and is sensitive to hydrogen fluids within samples [13]. Therefore, NMR methods can probe the total pore space in the sample using transverse relaxation times (T_2) and other NMR signals [27].

The previous literature has shown that SEM observations, mercury intrusion, CT scanning, and NMR can predict pore structures in unconventional oil and gas reservoirs, and explains weak connectivity and low recoveries to some extent [11, 24, 28]. NMR can explain moveable fluid saturation, and MIP can describe connectivity. However, effective fluid movability analysis for tight sandstone reservoirs has rarely been reported. This study has investigated pore-structure characterization methods and effective fluid movability for tight sandstone reservoirs. For this work, several tight sandstone samples were collected, and several techniques, including MIP, SEM, CT scanning, and NMR, were used to infer pore structure, pore connectivity, and effective fluid recoverability of the tight sandstone reservoir in the Upper Triassic Yanchang Formation Chang 7 Member, Ordos Basin. These analyses together will provide a better understanding of pore-structure characterization and pore connectivity in tight sandstones, enabling efforts to enhance recovery in these tight reservoirs.

2. Geological Background

Recently, great breakthroughs in unconventional oil and gas production in the Ordos Basin are focused on tight sandstone reservoirs. The Ordos Basin was formed on the western side of the North China platform, which is the second largest oil-bearing sedimentary basin in China [29]. The study area is located in the midwestern part of the Yishan slope, in the Ordos Basin (Figure 1(a)). The structure of the Chang 7 Member is a westward-dipping monocline, with a dip angle of 0.5 [30]. Oil and gas production in the Ordos Basin has increased rapidly year by year, and the leading tight sandstone formations (the Chang 7 Member of the Mesozoic Triassic Yanchang Formation) in the Ordos Basin have contributed approximately 20×10^8 tons to the geological reserve [31].

The thickness of the Chang 7 Member in the study area is about 80 and 120 m, and it can be divided into three layers based on the lithology. The tight sandstone reservoirs are mainly distributed in the Chang 7_1 and Chang 7_2 layers of the local area, where subaqueous distributary channels and estuarine dam microfacies of the delta front have developed. The Chang 7_3 layer is a major hydrocarbon source in Mesozoic oil-bearing systems [32, 33]. The tight sandstone of the Chang 7 Member, which formed at the most expansive stage of the lacustrine basin, is lithologically complex and dominated by fine sandstone, siltstone, and argillaceous siltstone (Figure 1(b)). The tight sandstone reservoir is adjacent to a widely distributed hydrocarbon source and is characterized by tight, poor physical properties and high source-reservoir matching [34].

3. Materials and Methods

3.1. Samples and Preparation. Samples were taken from the tight sandstone reservoir of the Upper Triassic Yanchang Formation, Chang 7 Member in the Dingbian area, Ordos Basin. Three typical cylindrical plug samples were drilled from two drilling cores, parallel to the formation (Figure 1(a)), with a diameter of 25 mm. The lithology of the samples was siltstone and fine sandstone. Each sample was divided into several pieces for a series of experiments, including porosity and permeability tests, SEM, MIP, CT scanning, and NMR to characterize their pore structure, pore connectivity, and movable fluid distribution. Alcohol was used remove residual asphalt from the samples before the experiments commenced. The samples were dried at 110°C for more than 24 hours until constant weight, placed in a drying dish, and cooled to 25°C to avoid moisture readsorption.

3.2. Experiments

3.2.1. Scanning Electron Microscopy (SEM). A JSM-6610LV scanning electron microscope was used to observe the micro- and nanopores of the samples at high resolution, with an acceleration voltage of 15 kV, a temperature of 20°C, and a relative humidity of 50%. Minerals around the pores were analyzed using an IE250 energy-dispersive X-ray spectrometer. The freshly polished surface of each sample was observed under an electron microscope.

3.2.2. Porosity and Permeability. Porosity and permeability analysis of each sample was carried out using the gas-pulse attenuation method, using an AP-608 automatic permeability-porosity tester with a minimum porosity of 0.1% and a minimum permeability of 0.001 mD. Firstly, dry samples were placed in the core clamping device, and helium gas was allowed to isothermally expand into the sample until equilibrium. Porosity was calculated by the grain volume and bulk

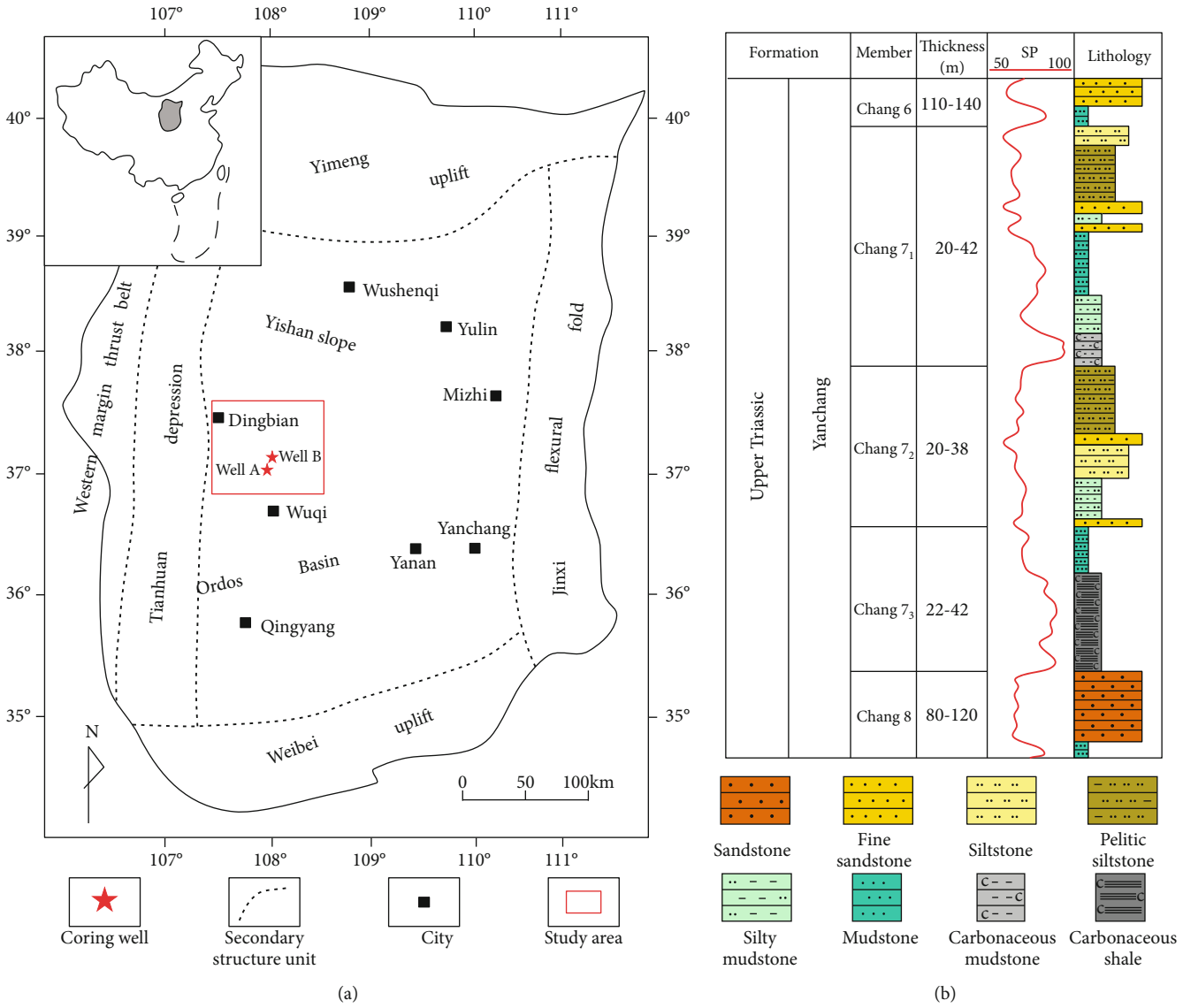

Figure 1: Structural and coring well locations in the Ordos Basin (a) and schematic of the lithology profile of the Upper Triassic Yanchang Formation, Chang 7 Member (b).

volume of the sample, and the average value after three tests was selected [8]. Gas permeability was measured by the unsteady-state pulse decay technique and the average value was used. The experimental operating procedure was in conformity with the SY/T 5336-2006 standard conventional core analysis method used by the Chinese oil and gas industry.

3.2.3. Mercury Intrusion Porosimetry (MIP). Dry samples were subjected to MIP immediately after porosity and permeability tests, using an AuToPoRE IV 9500 mercury intrusion meter (McMurray) according to SY/T 5346-2005 standards. Mercury injection pressures ranged from 0.004 to 208 MPa, giving a corresponding pore-throat radius of 0.003 μm. When the pressure gradually recovered to zero, sample mercury intrusion and mercury withdrawal capillary pressure curves were obtained. Then, the pore-throat size distribution could be obtained using the Washburn model based on mercury volume at different pressures [35]:

$$P_c = \frac{2\sigma \cos\theta}{r_c}, \quad (1)$$

where P_c is the mercury entry pressure, psi; σ is the interfacial tension (485 mN/m); θ is the contact angle (140°); and r_c is the corresponding pore-throat radius, μm.

3.2.4. Microcomputer Tomography (Micro-CT). A sample can be analyzed nondestructively using the CT scanning technique, and 3D pore distribution data can be obtained by 3D digital reconstruction based on sample scanning slices [36]. Micro-CT was carried out on the high-resolution 3D X-ray microXCT-400 imager, produced by Xradia, USA, with a maximum theoretical 3D spatial resolution of less than

1 μm. The procedure refers to the ACTIS/600 industrial CT operation manual. Firstly, X-rays were focused, by an optical lens, through the sample. X-ray penetration was measured by a specific detection device, and 2D scanning slices of the sample section were generated. Then, 2D scanning slices were reconstructed by the 3D model using the 3D modeling image-processing software. Next, a density distribution reconstruction map was obtained for the sample, enabling visual analysis of the 3D space of internal pores in the core.

3.2.5. Nuclear Magnetic Resonance (NMR). Nuclear magnetic resonance (NMR) nondestructively analyzes pore characteristics and the fluid distribution of samples, based on correlations between the movement of hydrogen atoms in water or hydrocarbon fluids and pores in rocks [37]. This experiment was carried out on a MacroMR12-150H-I NMR instrument produced by Newman, with the maximum number of echoes in the CMPG being 18,000 and the shortest echo time being less than 420 μs. Experiments were carried out in two groups, one in 100% saturated water and the other in bound water. All samples were thoroughly saturated with saline (80 g/l KCl) for several days before testing until the weight no longer increased, and then samples in a saturated-water state were tested to obtain the T_2 distribution. Next, to achieve the ideal bound-water state, samples were centrifuged at 417 psi to achieve the optimal centrifugal force corresponding to a throat radius of 0.05 μm [38], which is the lower throat radius limit for a movable fluid. Then, the second set of samples was tested to obtain the T_2 distribution in the bound-water state. The volume relaxation and diffusion relaxation terms of the fluid are usually negligible for NMR applications in petroleum, and therefore, the relaxation time T_2 can be approximated as

$$\frac{1}{T_2} = \rho_2 \frac{S}{V}, \tag{2}$$

where T_2 is the transverse relaxation time, ms; ρ_2 is the transverse surface relaxation strength, μm/ms; and S/V is the specific surface of a single pore, $\mu m^2/ms^3$.

Previous studies have shown through a large number of statistical experiments that T_2 has a power function relationship with the PSD [39, 40]. The relationship between the specific surface and the pore diameter is $S/V = F_s/\gamma$ for spherical and columnar pore-structure simplifications. In addition, $C = \rho_2 F_s$, and

$$\gamma = C * T_2{}^n, \tag{3}$$

where γ is the pore radius, μm; F_s is the single-pore shape factor; and n is the power exponent.

4. Results

4.1. Pore Morphology by SEM. Pores were identified through SEM observation and classified into three types: residual interparticle pores, intergranular pores, and dissolution pores (Figure 2). Residual interparticle pores were rare because of strong compaction and diagenesis, but intergranular pores in different minerals were relatively large in number. The size of these intergranular pores is generally controlled by the size and shape of mineral crystals and was typically less than 1 μm (Figures 2(c)–2(f)). Typical clays found in these samples were chlorite (Figure 2(a)), mica (Figure 2(b)), mixed-layer illite and smectite (Figure 2(c)), and kaolinite (Figure 2(e)). Dissolution pores included both intergranular and intragranular dissolution pores and were the most important pore type in the study area (Figures 2(g) and 2(h)). Furthermore, dissolution pores mainly originated from the dissolution of feldspar, and occasionally feldspar leaching was seen (Figure 2(i)).

The surface porosity of these samples ranged from 0.97% to 1.83%, with the average being 1.19% (Figure 3). Dissolution pores in feldspar contributed most to the range from 0.20% to 0.95%, with the average value being 0.52%. Interparticle and intergranular pores contributed to a smaller range from 0.27% to 0.76%, with the average being 0.48%, and the average was 0.09% for lithic fragment pores.

4.2. Petrophysical Properties and PSD by MIP. Petrophysical property test results showed that the porosity of the collected samples ranged from 2.98% to 10.90%, with an average of 7.39%, and the permeability ranged from 0.004 to 0.194 mD, with an average of 0.1 mD (Table 1). The Chang 7 reservoir is a typical tight sandstone reservoir because it has low porosity and permeability.

Figure 4(a) shows the intrusion-extrusion curves obtained by MIP. All curves are S-shaped, with no horizontal steps. The average displacement pressure was 2.06 MPa, and the injected mercury pressure started to rise sharply around 20 MPa. The median saturation pressure of sample DT40 was 205.44 MPa, which was much higher than the 8.96 MPa and 11.12 MPa obtained for samples DT18 and DT44, respectively. However, the mercury input saturations of the three samples differed greatly. The highest mercury input saturation was seen in sample DT18, with a value of 72.40%, and the lowest was seen in sample DT40, with a mercury input saturation of only 40.35%. The mercury removal efficiency of each sample was relatively low, with an average value of 26.8% (Table 1). Results showed that the average throat radius of the samples was 0.11 μm and that pore space was mainly contributed by pores within the 10–500 nm range, with pores of <10 nm and >0.5 μm making very little contribution (Figure 4(b)).

4.3. PSD by NMR T_2 Spectrum. According to the principle of NMR, the NMR signal strength of the hydrogen atoms in the fluid inside the pores of porous media is proportional to the size of the pores [37]. This means that the T_2 value reflects the pore radius and that the amplitude of the T_2 spectrum represents the content of the pores. Therefore, the NMR T_2 spectrum of samples measured under saturated single-phase fluid conditions can reflect the distribution of total pores, including connected and disconnected pores.

Figure 5 shows the NMR T_2 spectrum of each sample in a saturated-water state. The T_2 values mainly ranged from 0.1 ms to 200 ms, 0.1 ms to 100 ms, and 0.1 ms to 1000 ms. All T_2 sample spectra showed a bimodal pattern, with the

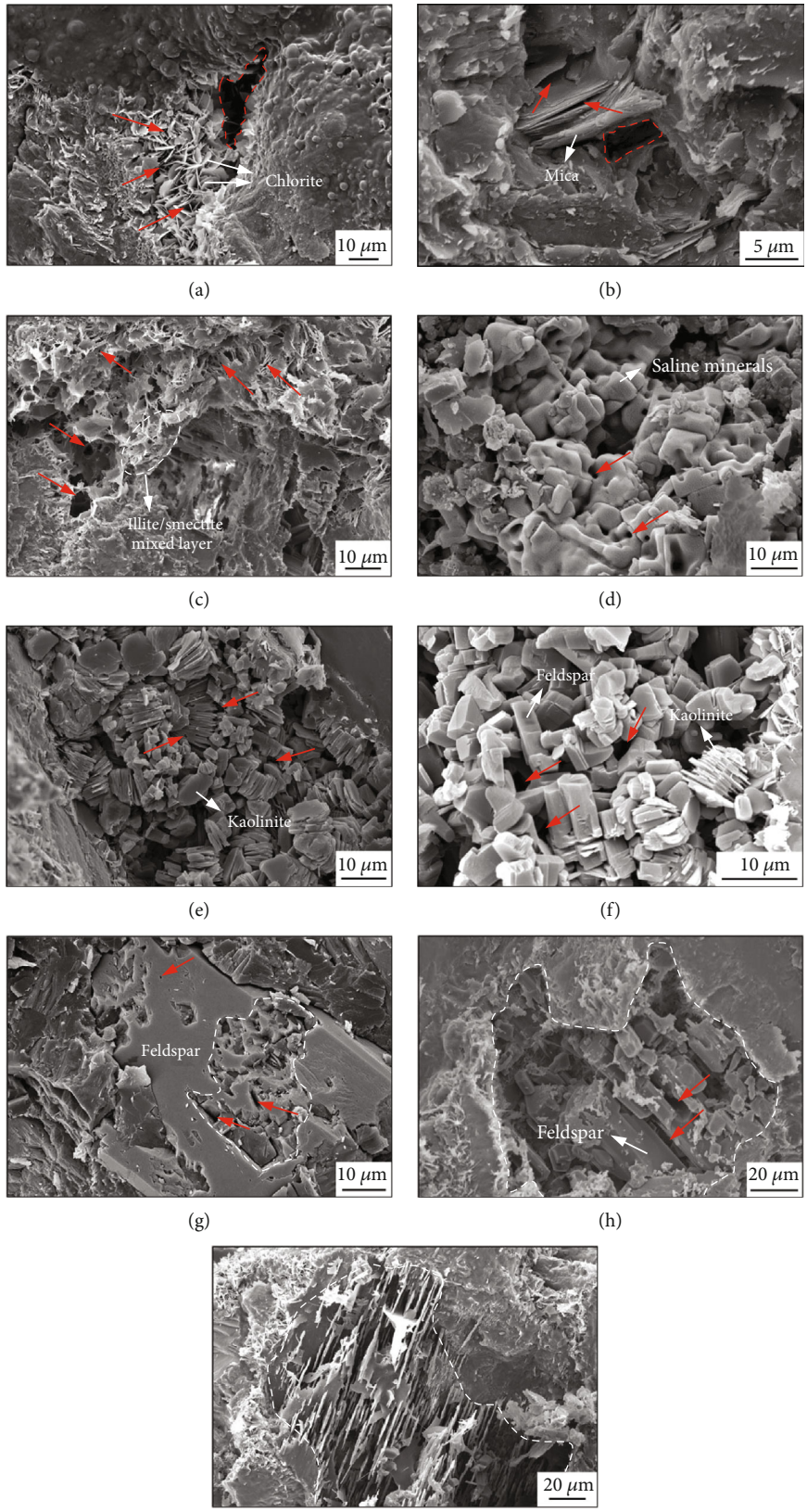

Figure 2: SEM images of different types of pores in tight sandstones. (a) Residual interparticle pores. (b) Intergranular pores in mica. (c) Intergranular pores in illite/smectite. (d) Intergranular pores in saline minerals. (e) Intergranular pores in kaolinite. (f) Interparticle pores in feldspar. (g, h) Dissolution pores in feldspar. (i) Feldspar leaching.

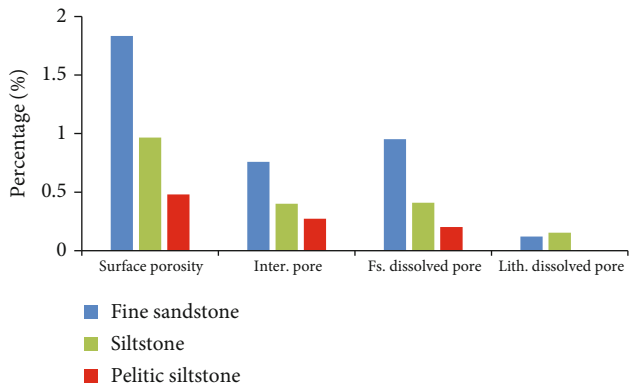

Figure 3: Surface porosity and its percentage values for different types of pores from SEM images. Inter.: interparticle and intergranular; Fs.: feldspar; Lith.: lithic fragments.

amplitude of the left peak being higher than that of the right peak. The inflection point was near $T_2 = 10$ ms, and the peak was near $T_2 = 1$ ms. In general, the collected samples contained mainly small pores ($r < 0.05\,\mu$m) based on the basic principle of positive correlation between the T_2 value and pore size, whereas the PSDs of large pores ($r > 0.05\,\mu$m) were different. In particular, sample DT44 contained more than 40% large pores.

4.4. 3D Pore Distributions from Micro-CT. Figures 6(a)–6(c) illustrate 2D CT scanning slices of each sample, with the pores and the matrix represented by different grayscale values and black points representing the pores. Figures 6(d)–6(f)show the 3D distributions of pore space based on 780 continuous 2D scanning slices, with the pores represented in red. The results show that the pores of sample DT18 were distributed mostly in scattered states (Figure 6(d)) and were most developed on the plane (Figure 6(a)). Only a few small pores were developed in sample DT40 (Figures 5(b) and 6(e)). Some larger pores were developed in sample DT44, corresponding with the NMR results (Figures 5(c) and 6(f)). Slight bedding can be seen in sample DT44 (Figure 6(c)), and the 3D pore distribution shows a certain stratification with a zonal distribution (Figure 6(f)). Some researchers believe that the development of bedding can improve rock permeability to a certain extent, accompanied by the formation of larger pores or microfractures [13, 41]. However, the 3D pore distributions in each sample show large numbers of isolated pores, which cannot provide an effective channel for oil and gas migration. Pore connectivity will be discussed further in the following chapters.

5. Discussion

5.1. Pore Connectivity Analysis

5.1.1. Full PSD Calculated by MIP and NMR. The capillary pressure curves and the NMR T_2 spectra were both directly related to pore-structure characteristics for the same sample. The PSD from NMR was calculated from the T_2 spectrum with reference to the literature based on the theory discussed in Section 3.2.5 [40]. Figure 7 shows the conversion between the NMR T_2 spectrum and the pore-throat radius. According to the principle of MIP, mercury preferentially enters the larger connected pore throats with increasing displacement pressure. Hence, volume information can be obtained only for pores below the maximum mercury injection pressure, whereas the NMR T_2 spectrum reflects the total pore space. For conversion accuracy, pore-throat radii below the maximum mercury saturation were chosen for interpolation calculations with the T_2 spectrum. The error-minimizing values of C and n were obtained by fitting $r(i) \sim T_2(i)$ according to the least-squares principle. By substituting the result into Equation (3), the PSD can be obtained from NMR. The conversion coefficients of the samples are presented in Table 2.

5.1.2. Comparison of PSD between NMR and MIP. Figure 8 shows the PSDs obtained by NMR and MIP. For the sake of comparison and analysis, one-to-one correspondence between the pore sizes of each measurement was used. This showed that the maximum pore radii obtained by NMR and MIP were both less than 1 μm and that the PSD from NMR was generally greater than that from MIP.

According to the results from NMR, the pore sizes were concentrated in two ranges: pores less than 100 nm (period I) and pores greater than 100 nm (period II). The nanoscale pores ranging from 10 nm to 100 nm in period I were relatively well developed and contributed about 75.6%–92.1% to the total pore volume of these samples, whereas the pores of period II contributed about 7.9%–24.4% to the total pore volume. This indicated that nanoscale pores provide extremely important reservoir space for tight sandstone reservoirs in the study area. PSD from MIP illustrated that the connected pores mainly ranged from 10 to 500 nm.

Note that the amplitude of the MIP curve is higher than that of the NMR curve around 100 nm for sample DT40. The cause of this phenomenon is due to the influence of the testing principle. MIP is primarily sensitive to throats, not pores. The PSD obtained by MIP reflected the total volume of all throats and their connected pores under a certain pressure. However, there was no displacement process during the NMR experiment. The PSD obtained by NMR represented the total volume of all throats and pores with a certain radius, whether connected or not.

5.1.3. Quantitative Characterization of Pore Connectivity. The PSD from MIP calculated from the volume of mercury at different pressures reflects the connected pores that mercury can invade. In contrast, the PSD obtained from NMR shows the total pore-volume distribution because disconnected pores are also filled with fluid. Therefore, the PSD from NMR is generally greater than that from MIP, and the difference between them is distinct in tight sandstones [13, 14]. The authors think that this gap represents the disconnected pores in sandstones (Figure 8).

This paper proposes that the pore connectivity percentage (PCP) is the ratio of the cumulative pore volume obtained by MIP to the cumulative total pore volume obtained by NMR in a certain pore-throat radius range. On

Table 1: Petrophysical characteristic parameters of selected samples.

Sample	Well	Depth (m)	Subsection	Poro (%)	Perm (mD)	MIP				
						P_t (MPa)	P_{50} (MPa)	S_{max} (%)	S_r (%)	r_a (μm)
DT18	Well A	2221.73	Chang 7	10.90	0.102	1.83	8.20	72.40	30.94	0.12
DT40	Well B	2294.34	Chang 7	2.98	0.004	2.86	205.44	40.35	22.17	0.08
DT44	Well B	2295.10	Chang 7	8.28	0.194	1.49	10.26	60.35	27.28	0.15

Note: Poro: porosity; Perm: permeability; P_t: displacement pressure of mercury injection; P_{50}: pressure of median mercury saturation; S_{max}: maximum intrusion mercury saturation of sample; S_r: extrusion mercury saturation of sample; r_a: average throat radius of sample.

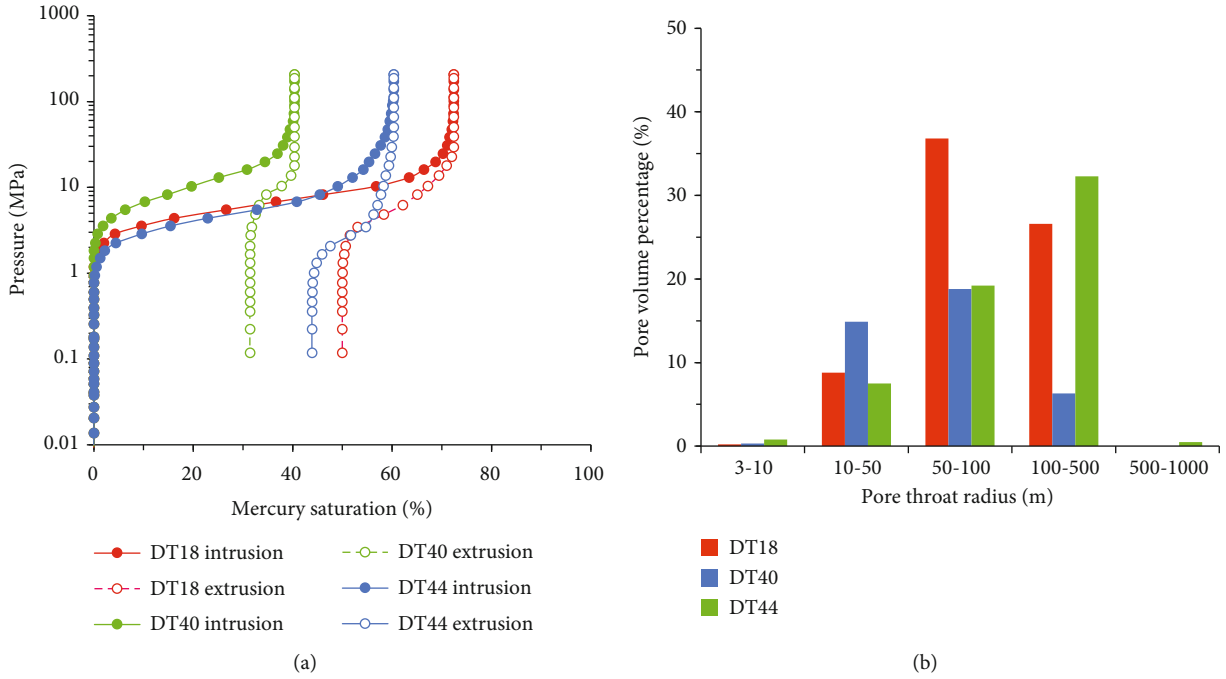

Figure 4: High-pressure mercury intrusion-extrusion curves (a) and pore-size distribution of selected samples (b).

this basis, the PCP of total pore space and pores of different radii (<50 nm, 50 nm–0.1 μm, and 0.1 μm–1 μm) of the three sandstone samples were calculated by MIP and NMR (Table 3). Moreover, 50 nm is the lowest throat-radius limit for movable fluid, whereas 0.1 μm is the dividing point between periods I and II from NMR.

The results showed that the pore volume by NMR of the tight sandstone samples ranged from 0.0011 ml/g to 0.0219 ml/g, with an average value of 0.0101 ml/g (Table 3). The total PCPs of the tight sandstone samples were relatively low, with values of 25.11%, 36.30%, and 24.25% (Table 3). The PCP varied dramatically when the pore radius was greater than 50 nm (the cutoff point). The PCP increased at larger pore radii, varying from 36.60% to 92.00% with an average value of 63.68% in the pore-size ranges of 50 nm < r < 0.1 μm and r > 0.1 μm (Figure 9(b)). However, the connectivity of pores less than 50 nm was extremely poor, with values ranging from 5.02% to 18.18% (Figure 9(b)). Nevertheless, pores in this same range accounted for most of the pore volume of each sample, ranging from 0.0099 ml/g to 0.0219 ml/g, with an average value of 0.0173 ml/g (Figure 9(a)). In other words, tight sandstone has a great many disconnected pores. The reason for this phenomenon may be that the tight sandstones in the study area are delta front subfacies and are mainly composed of fine particles with strong sorting, which makes nanoscale and microscale pores dominate in the tight sandstone samples [29, 30, 34]. In addition, during densification of sedimentary rock, finer particles were more likely to form dead pores, resulting in low connectivity.

5.2. Movable Fluid Analysis

5.2.1. T_2 Cutoff Values and Movable Fluids. The T_2 cutoff was the key parameter for calculating movable fluid saturation in the NMR experiment, the left side of the T_2 cutoff represents bound fluid, and the right side represents movable fluid [42]. The T_2 cutoff varied according to differences in the specific surface area of each sample [43]. Figure 10 shows the method of calculating the T_2 cutoff value. First, the cumulative proportion of the T_2 spectrum under saturated water (CPS) and irreducible water (CPI) conditions was obtained. Then, a horizontal line was drawn starting from the maximum CPI and intersecting with the CPS at a point. The corresponding T_2 value at that point was the T_2 cutoff value.

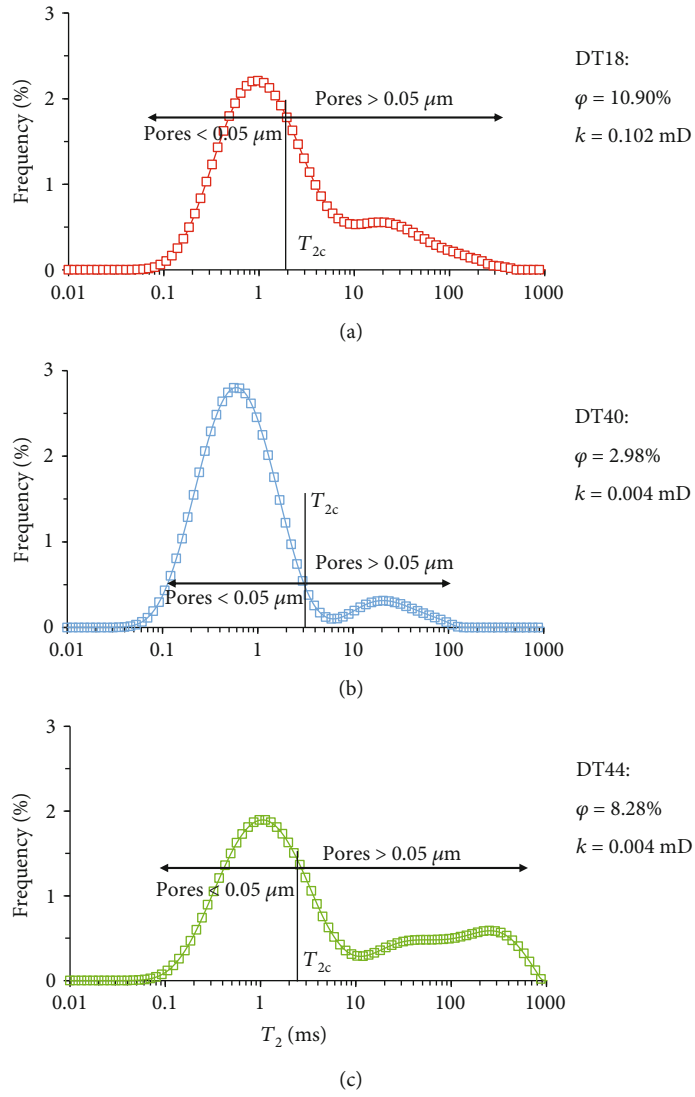

Figure 5: Characteristics of the T_2 spectrum of samples under water-saturated conditions.

The calculation results showed that the T_2 cutoff values of the samples ranged from 1.70 ms to 3.18 ms, which were less than the empirical value (13 ms) for low-permeability reservoirs. The movable fluid saturation of the three tight sandstone samples was obtained from the T_2 cutoff values (Table 4). The movable fluid saturation is mainly used to characterize the fluid movability of reservoirs, which represents the proportion of the volume of movable fluid to the total pore volume. The movable fluid saturations of the samples (DT18, DT40, and DT44) were 43.01%, 10.20%, and 40.09%, respectively. The value of sample DT40 was much lower than that of the other two samples, indicating that the fluid movability of sample DT40 was extremely low.

5.2.2. Effective Movable Fluid. Movable fluids were calculated through the T_2 cutoff values of the samples, and movable fluids occurred in pores greater than 50 nm. These pores included both connected and disconnected pores. The pore volume at a scale greater than 50 nm can be divided into three conditions. The first includes pores connected by an adjacent throat (>50 nm), where fluids can break through during centrifugation (Figure 11(a)). The second condition includes pores connected by an adjacent throat (<50 nm), but where fluids cannot break through the throat during centrifugation (Figure 11(b)). The third condition includes isolated pores without a connecting throat, from which fluids cannot be centrifuged out. The fluid in isolated pores was retained during rock deposition and diagenesis and prevented pore collapse at high pressure [14]. Therefore, it was not accurate to use the initial movable fluid saturation calculated using the NMR T_2 cutoff value to evaluate fluid movability. The effect of disconnected pores on movable fluid saturation should be excluded.

The pores that mercury could invade were all the connected pores under a certain displacement pressure from the MIP experiment [13]. When the displacement pressure corresponding to the cutoff throat radius (F_c) was higher than the capillary pressure (F_i) (Figure 11(c)), the pore volume that mercury could invade was identical to the first condition discussed above (Figure 11(a)). On the contrary, the

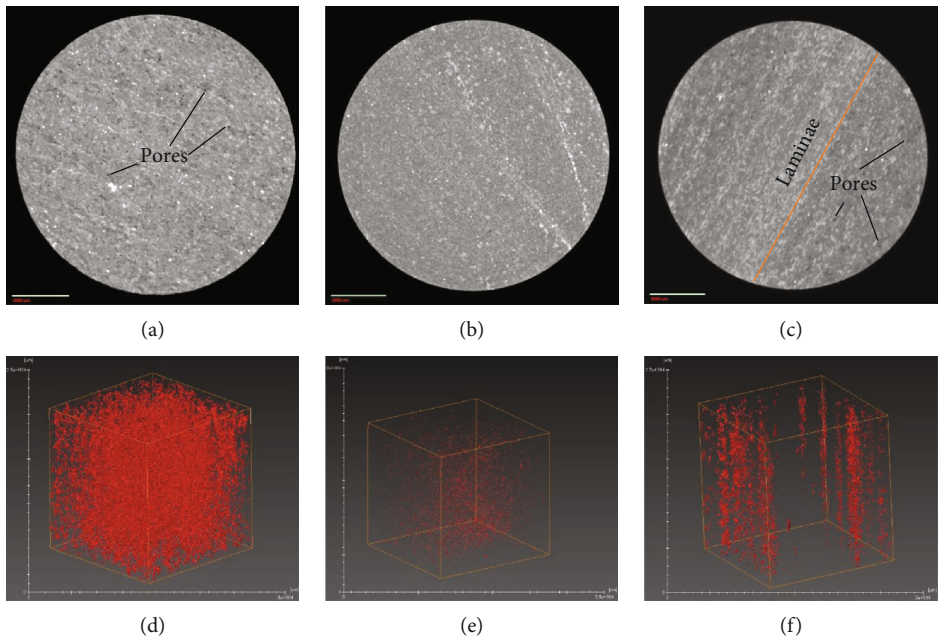

Figure 6: 2D and 3D pore distribution characteristics by CT scanning. (a, d) Experimental results for sample DT18. (b, e) Experimental results for sample DT40. (c, f) Experimental results for sample DT44.

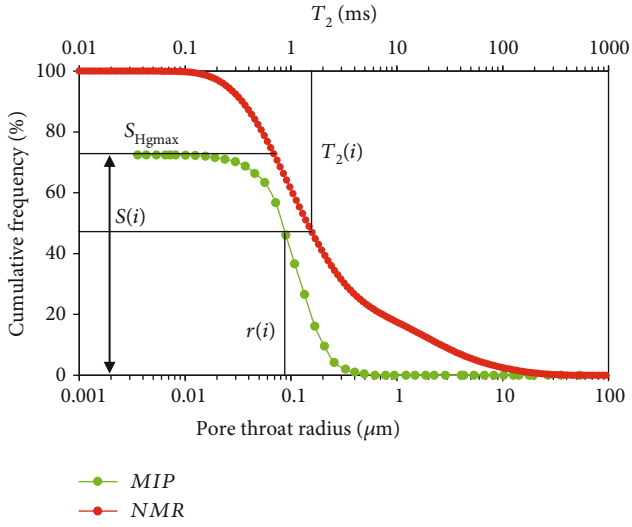

Figure 7: Sample DT18 showing the conversion between NMR T_2 spectrum and pore-throat radius. S_{Hgmax}: maximum mercury saturation; $r(i)$: pore-throat radius; $S(i)$: cumulative frequency corresponding to $r(i)$; $T_2(i)$: T_2 corresponding to $S(i)$.

Table 2: T_2 conversion coefficients of selected samples.

Sample	C	n	R^2
DT18	42.52	0.47	0.86
DT40	41.90	0.45	0.90
DT44	22.09	0.52	0.83

rest of the connected pore volume conformed to the second condition (Figure 11(d)) when F_c was less than F_i (Figure 11(b)).

Therefore, a new parameter, effective movable fluid saturation (S_e), was proposed on the basis of the physical concepts of movable fluid saturation and pore connectivity. It represents the ratio of pore-throat volume greater than the cutoff throat radius to total pore volume in a unit volume and is equal to the initial movable fluid saturation (S_i) times the pore connectivity percentage (β) greater than the cutoff pore-throat radius:

$$S_e = \beta * S_i, \tag{4}$$

where S_e is the effective movable fluid saturation, %; S_i is the initial movable fluid saturation, %; and β is the connectivity percentage of pores greater than the cutoff pore-throat radius, which is a constant.

The effective movable fluid saturations of the three tight sandstone samples were calculated using Equation (4). S_e ranged from 8.78% to 24.63%, with an average of 16.94% (Figure 12). These results show that the initial movable fluid saturation (S_i) decreased by 14.16% on average after eliminating disconnected pores. It can be concluded from this that the low recovery of tight sandstone reservoirs is due to the heterogeneity and weak connectivity of tight sandstones. It is essential to exclude disconnected pores when calculating the recovery of a reservoir. Effective movable fluid saturation is a comprehensive reflection of pore structure and fluid distribution characteristics, which is a positive step towards exploitation and productivity evaluation of tight sandstone reservoirs.

6. Conclusions

Multitechniques were used to characterize the pore structure of tight sandstone. Pore connectivity and movable fluid

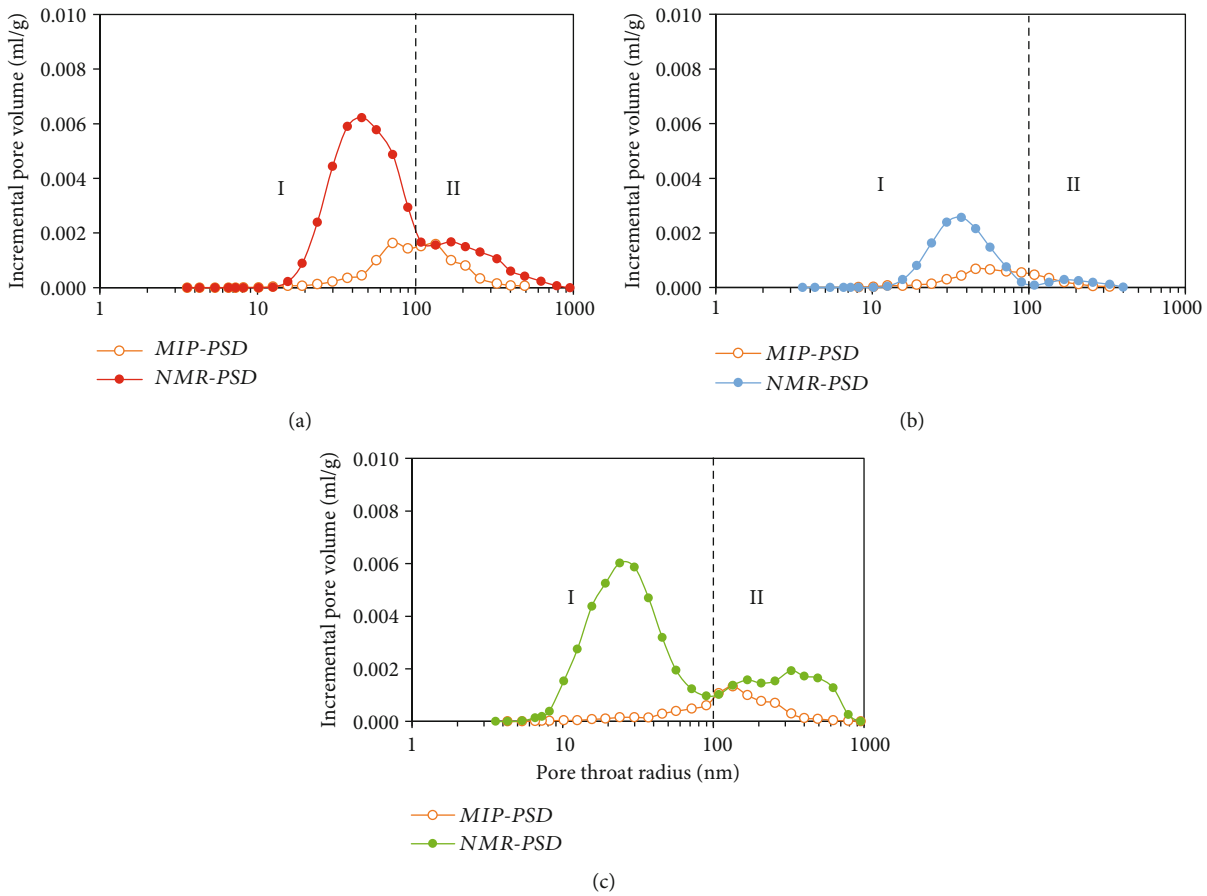

Figure 8: Comparison of PSDs between MIP and NMR.

Table 3: Pore volume by NMR and pore connectivity percentage by MIP and NMR.

Sample	Pore volume by NMR (ml/g)			Pore connectivity percentage (%)			
	<50 nm	50 nm–0.1 μm	>0.1 nm	<50 nm	50 nm–0.1 μm	>0.1 nm	Total
DT18	0.0201	0.0153	0.0084	6.97	36.60	47.62	25.11
DT40	0.0099	0.0025	0.0011	18.18	92.00	72.73	36.30
DT44	0.0219	0.0033	0.0081	5.02	78.79	54.32	24.25

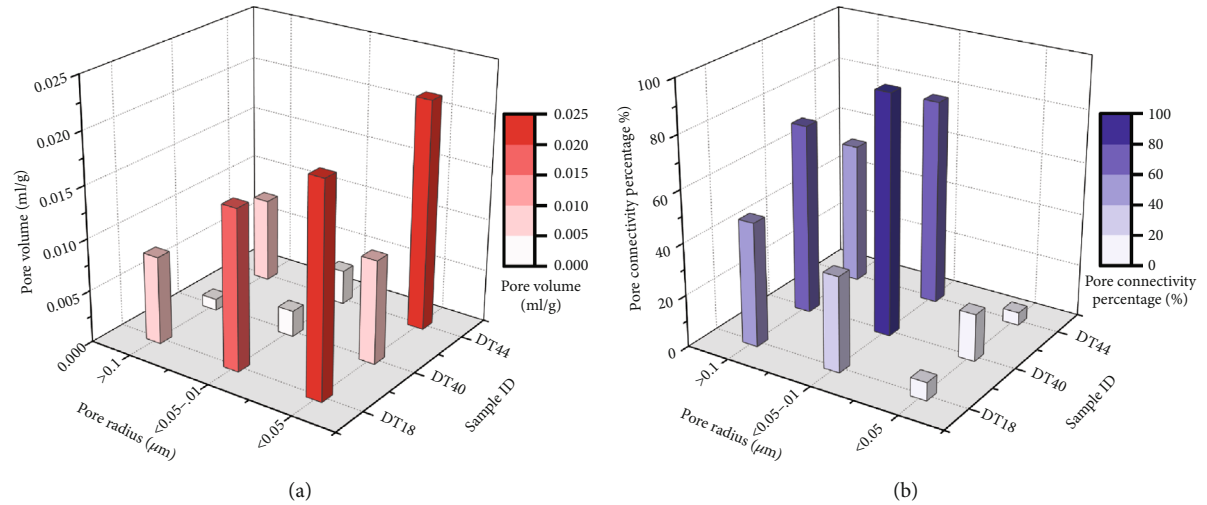

Figure 9: Pore volume by NMR (a) and pore connectivity percentage by MIP and NMR (b).

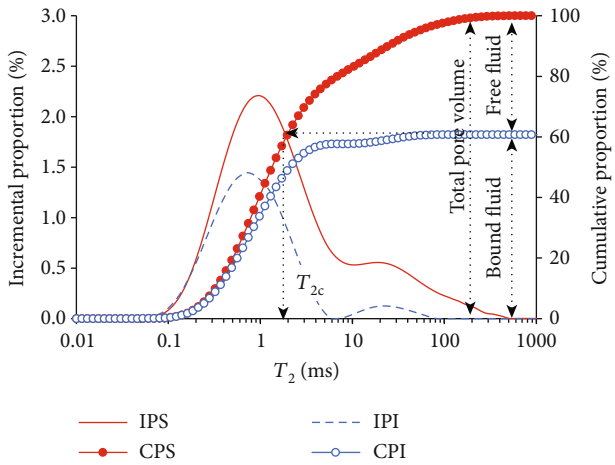

FIGURE 10: Illustration of the method to calculate the T_2 cutoff value (T_{2c}) using sample DT18. IPS: incremental proportion at saturated-water condition; IPI: incremental proportion at irreducible water condition; CPS: cumulative proportion at saturated-water condition; CPI: cumulative proportion at irreducible water condition.

TABLE 4: T_2 cutoff and movable fluid saturation from NMR measurements.

Sample	Len (cm)	Dia (cm)	Wt_w (g)	Wt_d (g)	NMR T_{2c} (ms)	S_m (%)
DT18	3.45	2.49	41.28	40.29	1.70	43.01
DT40	3.97	2.47	50.28	49.64	3.18	10.20
DT44	3.67	2.48	45.16	44.44	2.58	40.09

Note: Len: length; Dia: diameter; Wt_w: wet weight; Wt_d: dry weight; S_m: movable fluid saturation.

distribution were characterized quantitatively based on MIP and NMR. The main findings of this work can be summarized as follows:

(1) SEM observation showed that the main pore types for tight sandstones are interparticle pores between different minerals and dissolved pores in feldspar, with most pores smaller than 1 μm. The 3D pore distribution from micro-CT results showed some stratification with a zonal distribution

(2) The PSD from NMR showed that pore sizes were concentrated in two ranges: less than 100 nm (period I) and greater than 100 nm (period II). PSD from MIP showed that the connected pores mainly ranged from 10 to 500 nm. PSD comparison between NMR and MIP indicated that PSD from NMR is generally greater than that from MIP because MIP characterizes only the volume of connected pores, whereas NMR shows the volume of all pores

(3) Tight sandstones have weak connectivity percentages, 28.6% on average. Movable fluids are mainly distributed in pores over 50 nm, and these pores have higher connectivity percentages ranging from 36.6% to 92.0%, although they have smaller pore volume

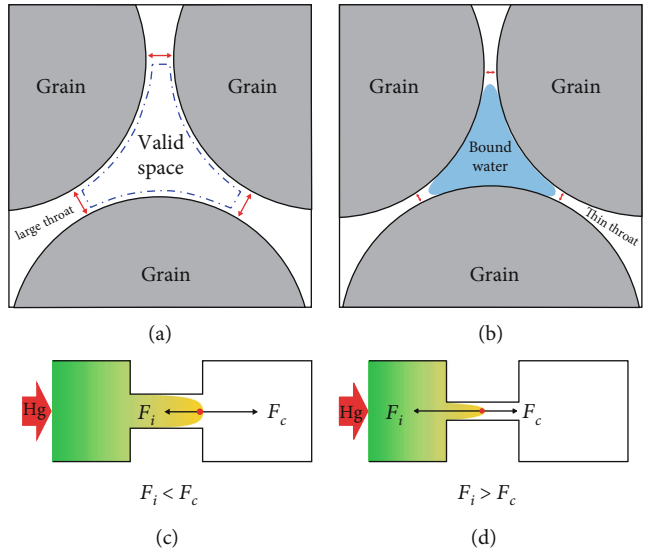

FIGURE 11: Distribution of movable fluids in pores and mercury injection of connected pores. Valid pore space (first condition) for movable fluid (a); void pore space (second condition) for bound water (b); pores with a throat greater than 50 nm (first condition) that mercury can invade (c); pores with a throat less than 50 nm (second condition) that mercury cannot invade (d). F_i: capillary pressure; F_c: displacement pressure corresponding to the cutoff throat radius.

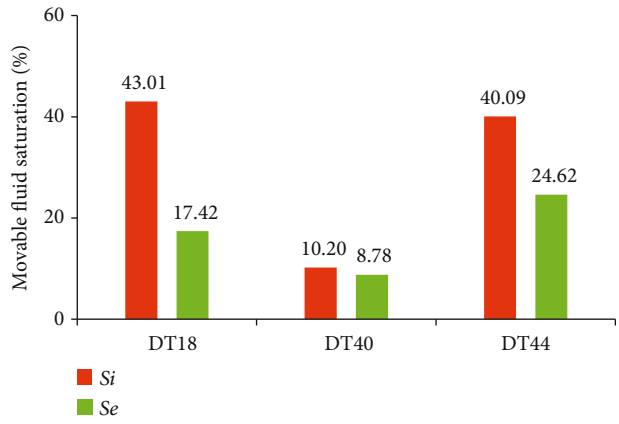

FIGURE 12: Comparison between an effective movable fluid (S_e) and initial movable fluid (S_i).

(4) A new parameter, effective movable fluid saturation (S_e), was proposed based on the initial movable fluid saturation (S_i) from NMR and the pore connectivity from MIP and NMR. The effective movable fluid saturation (S_e) was calculated for three tight sandstone samples, and it was found that the movable fluid saturation decreased by 14.16% on average when unconnected pores were excluded

Data Availability

The data used to support the findings of this study are available from the corresponding authors upon request.

Conflicts of Interest

The authors declare that they have no conflict of interest.

Acknowledgments

This study was supposed by the National Science and Technology Major Project (2016ZX05034002-006), the National Natural Science Foundation of China (41972137), the Science and Technology Innovation Planning Project of Shaanxi Province of China (2016KTCL01-12), and the Independent Project of the State Key Laboratory of Oil and Gas Reservoir Geology and Exploitation. The authors greatly thank the Research Institute, Shaanxi Yanchang Petroleum (Group) Co., Ltd., for providing all the core samples and related data.

References

[1] Z. Yang and C. Zou, "'Exploring petroleum inside source kitchen": connotation and prospects of source rock oil and gas," *Petroleum Exploration and Development*, vol. 46, no. 1, pp. 181–193, 2019.

[2] F. Hao, H. Zou, and Y. Lu, "Mechanisms of shale gas storage: implications for shale gas exploration in China," *AAPG Bulletin*, vol. 97, no. 8, pp. 1325–1346, 2013.

[3] J. B. Curtis, "Fractured shale-gas systems," *AAPG Bulletin*, vol. 86, pp. 1921–1938, 2002.

[4] D. J. K. Ross and R. Bustin, "The importance of shale composition and pore structure upon gas storage potential of shale gas reservoirs," *Marine and Petroleum Geology*, vol. 26, no. 6, pp. 916–927, 2009.

[5] Q.-H. Hu, X.-G. Liu, Z.-Y. Gao, S.-G. Liu, W. Zhou, and W.-X. Hu, "Pore structure and tracer migration behavior of typical American and Chinese shales," *Petroleum Science*, vol. 12, no. 4, pp. 651–663, 2015.

[6] S. Peng and B. Loucks, "Permeability measurements in mudrocks using gas-expansion methods on plug and crushed-rock samples," *Marine and Petroleum Geology*, vol. 73, pp. 299–310, 2016.

[7] C. R. Clarkson, N. Solano, R. M. Bustin et al., "Pore structure characterization of North American shale gas reservoirs using USANS/SANS, gas adsorption, and mercury intrusion," *Fuel*, vol. 103, pp. 606–616, 2013.

[8] H. Xu, W. Zhou, R. Zhang, S. Liu, and Q. Zhou, "Characterizations of pore, mineral and petrographic properties of marine shale using multiple techniques and their implications on gas storage capability for Sichuan Longmaxi gas shale field in China," *Fuel*, vol. 241, pp. 360–371, 2019.

[9] W. Zhao, Y. Cheng, M. Yuan, and F. An, "Effect of adsorption contact time on coking coal particle desorption characteristics," *Energy & Fuels*, vol. 28, no. 4, pp. 2287–2296, 2014.

[10] R. Yang, F. Hao, S. He et al., "Experimental investigations on the geometry and connectivity of pore space in organic-rich Wufeng and Longmaxi shales," *Marine and Petroleum Geology*, vol. 84, pp. 225–242, 2017.

[11] H. Xu, W. Zhou, Q. Hu, X. Xia, C. Zhang, and H. Zhang, "Fluid distribution and gas adsorption behaviors in overmature shales in southern China," *Marine and Petroleum Geology*, vol. 109, pp. 223–232, 2019.

[12] M. G. Kibria, Q. Hu, H. Liu, Y. Zhang, and J. Kang, "Pore structure, wettability, and spontaneous imbibition of Woodford Shale, Permian Basin, West Texas," *Marine and Petroleum Geology*, vol. 91, pp. 735–748, 2018.

[13] F. Gao, Y. Song, Z. Li et al., "Quantitative characterization of pore connectivity using NMR and MIP: a case study of the Wangyinpu and Guanyintang shales in the Xiuwu basin, Southern China," *International Journal of Coal Geology*, vol. 197, pp. 53–65, 2018.

[14] C. X. Ning, Z. X. Jiang, Z. Y. Gao et al., "Quantitative evaluation of pore connectivity with nuclear magnetic resonance and high pressure mercury injection: a case study of the lower section of Es3 in Zhanhua sag," *Journal of China University of Mining & Technology*, vol. 46, no. 3, pp. 578–585, 2017.

[15] H. Xu, W. Zhou, Q. Cao et al., "Differential fluid migration behaviour and tectonic movement in Lower Silurian and Lower Cambrian shale gas systems in China using isotope geochemistry," *Marine and Petroleum Geology*, vol. 89, pp. 47–57, 2018.

[16] K. L. Milliken, L. T. Ko, M. Pommer, and K. M. Marsaglia, "Sem petrography of Eastern Mediterranean sapropels: analogue data for assessing organic matter in oil and gas shales," *Journal of Sedimentary Research*, vol. 84, no. 11, pp. 961–974, 2014.

[17] G. R. Chalmers, R. M. Bustin, and I. M. Power, "Characterization of gas shale pore systems by porosimetry, pycnometry, surface area, and field emission scanning electron microscopy/transmission electron microscopy image analyses: examples from the Barnett, Woodford, Haynesville, Marcellus, and Doig units," *AAPG bulletin*, vol. 96, no. 6, pp. 1099–1119, 2012.

[18] L. M. Anovitz and D. R. Cole, "Characterization and analysis of porosity and pore structures," *Reviews in Mineralogy and Geochemistry*, vol. 80, pp. 61–164, 2015.

[19] Q. Zhang, Y. Dong, S. Liu, D. Elsworth, and Y. Zhao, "Shale pore characterization using NMR cryoporometry with octamethylcyclotetrasiloxane as the probe liquid," *Energy & Fuels*, vol. 31, no. 7, pp. 6951–6959, 2017.

[20] S. Tong, Y. Dong, Q. Zhang, D. Elsworth, and S. Liu, "Quantitative analysis of nanopore structural characteristics of lower Paleozoic shale, Chongqing (Southwestern China): combining FIB-SEM and NMR cryoporometry," *Energy & Fuels*, vol. 31, no. 12, pp. 13317–13328, 2017.

[21] M. Sun, B. Yu, Q. Hu et al., "Pore characteristics of Longmaxi shale gas reservoir in the northwest of Guizhou, China: investigations using small-angle neutron scattering (SANS), helium pycnometry, and gas sorption isotherm," *International Journal of Coal Geology*, vol. 171, pp. 61–68, 2017.

[22] Y. Wang, Y. Zhu, S. Chen, and W. Li, "Characteristics of the nanoscale pore structure in Northwestern Hunan shale gas reservoirs using field emission scanning electron microscopy, high-pressure mercury intrusion, and gas adsorption," *Energy & Fuels*, vol. 28, no. 2, pp. 945–955, 2014.

[23] R. Zhang, S. Liu, J. Bahadur et al., "Estimation and modeling of coal pore accessibility using small angle neutron scattering," *Fuel*, vol. 161, pp. 323–332, 2015.

[24] R. G. Loucks, S. C. Ruppel, X. Wang et al., "Pore types, pore-network analysis, and pore quantification of the lacustrine shale-hydrocarbon system in the Late Triassic Yanchang Formation in the southeastern Ordos Basin, China," *Interpretation*, vol. 5, no. 2, pp. SF63–SF79, 2017.

[25] A. Amann-Hildenbrand, A. Ghanizadeh, and B. M. Krooss, "Transport properties of unconventional gas systems," *Marine and Petroleum Geology*, vol. 31, no. 1, pp. 90–99, 2012.

[26] M. Sun, B. Yu, Q. Hu, R. Yang, Y. Zhang, and B. Li, "Pore connectivity and tracer migration of typical shales in South China," *Fuel*, vol. 203, pp. 32–46, 2017.

[27] S. Zhang, J. Yan, Q. Hu et al., "Integrated NMR and FE-SEM methods for pore structure characterization of Shahejie shale from the Dongying Depression, Bohai Bay Basin," *Marine and Petroleum Geology*, vol. 100, pp. 85–94, 2019.

[28] H. Tian, L. Pan, X. Xiao, R. W. T. Wilkins, Z. Meng, and B. Huang, "A preliminary study on the pore characterization of Lower Silurian black shales in the Chuandong Thrust Fold Belt, southwestern China using low pressure N_2 adsorption and FE-SEM methods," *Marine and Petroleum Geology*, vol. 48, pp. 8–19, 2013.

[29] H. Deng, X. Xie, K. Chen, C. Vij, Y. Pang, and H. A. Li, "Mineralogical characteristics of continental shale: a case study in Yan-Chang Formation, Ordos Basin," *Australian Journal of Earth Sciences*, vol. 65, no. 6, pp. 851–862, 2018.

[30] Y. Jingli, D. Xiuqin, Z. Yande, H. Tianyou, C. Meijuan, and P. Jinlian, "Characteristics of tight oil in Triassic Yanchang formation, Ordos Basin," *Petroleum Exploration and Development*, vol. 40, no. 2, pp. 161–169, 2013.

[31] Y. A. N. G. Hua, X. Liang, N. I. U. Xiaobing, F. Shengbin, and Y. Yuan, "Geological conditions for continental tight oil formation and the main controlling factors for the enrichment: a case of Chang 7 Member, Triassic Yanchang Formation, Ordos Basin, NW China," *Petroleum Exploration and Development*, vol. 44, no. 1, pp. 11–19, 2017.

[32] C. Zou, S. Pan, B. Horsfield et al., "Oil retention and intra-source migration in the organic-rich lacustrine Chang 7 shale of the Upper Triassic Yanchang Formation, Ordos Basin, central China," *AAPG Bulletin*, vol. 103, no. 11, pp. 2627–2663, 2019.

[33] Z. Chen, Q. Guo, C. Jiang et al., "Source rock characteristics and Rock-Eval-based hydrocarbon generation kinetic models of the lacustrine Chang-7 shale of Triassic Yanchang Formation, Ordos Basin, China," *International Journal of Coal Geology*, vol. 182, pp. 52–65, 2017.

[34] Z. Zhang, S. Chen, H. Yang et al., "RETRACTED: Tight oil accumulation mechanisms of Triassic Yanchang Formation Chang 7 Member, Ordos Basin, China," *Petroleum Exploration and Development*, vol. 43, no. 4, pp. 644–654, 2016.

[35] J. Lai, G. Wang, Z. Fan et al., "Insight into the pore structure of tight sandstones using NMR and HPMI measurements," *Energy & Fuels*, vol. 30, no. 12, pp. 10200–10214, 2016.

[36] X. Liu, J. Wang, L. Ge et al., "Pore-scale characterization of tight sandstone in Yanchang Formation Ordos Basin China using micro-CT and SEM imaging from nm- to cm-scale," *Fuel*, vol. 209, pp. 254–264, 2017.

[37] C. Lyu, Z. Ning, Q. Wang, and M. Chen, "Application of NMRT2 to pore size distribution and movable fluid distribution in tight sandstones," *Energy & Fuels*, vol. 32, no. 2, pp. 1395–1405, 2018.

[38] Y. Wei, Y. Luo, Z. Yang, X. Liu, and X. Shi, "Studies on lithology characteristics and effective development mode of tight oil," in *Proceedings of the International Field Exploration and Development Conference 2017*, pp. 1639–1649, Springer, 2019.

[39] Y. D. He, Z. Q. Mao, L. Z. Xiao, and X. J. Ren, "An improved method of using NMR T_2 distribution to evaluate pore size distribution," *Diqiu Wuli Xuebao*, vol. 48, no. 2, pp. 373–378, 2005.

[40] A. F. Li, X. X. Ren, G. J. Wang, Y. Z. Wang, and K. L. Jiang, "Characterization of pore structure of low permeability reservoirs using a nuclear magnetic resonance method," *Journal of China University of Petroleum*, vol. 39, no. 6, pp. 92–98, 2015.

[41] X. Guo, Y. Shen, and S. He, "Quantitative pore characterization and the relationship between pore distributions and organic matter in shale based on nano-CT image analysis: a case study for a lacustrine shale reservoir in the Triassic Chang 7 member, Ordos Basin, China," *Journal of Natural Gas Science and Engineering*, vol. 27, pp. 1630–1640, 2015.

[42] Y. Yao and D. Liu, "Comparison of low-field NMR and mercury intrusion porosimetry in characterizing pore size distributions of coals," *Fuel*, vol. 95, pp. 152–158, 2012.

[43] H. Gao and H. Li, "Determination of movable fluid percentage and movable fluid porosity in ultra-low permeability sandstone using nuclear magnetic resonance (NMR) technique," *Journal of Petroleum Science and Engineering*, vol. 133, pp. 258–267, 2015.